Synthetic Biology and Engineering

SCIEPublish

Article

Elucidation of Diatom Impregnated with Iron Nanoparticles as a Bio-Stimulator in Early Growth and Development of Rice

Anwesha Mondal, Rahul Bose *, Santanu Paul and Ruma Pal

Department of Botany, University of Calcutta, Kolkata 700019, West Bengal, India; anwesha.mondal12@gmail.com (A.M.); spaul_1971@yahoo.com (S.P.); rpalcu7@gmail.com (R.P.)

* Corresponding author. E-mail: boserahul.89@gmail.com (R.B.)

Received: 28 May 2026; Revised: 27 July 2026; Accepted: 11 August 2026; Available online: 25 August 2026

ABSTRACT: Merging nanotechnology with biology, diatoms reveal an extraordinary capacity to fabricate iron nanoparticles (INPs) while simultaneously acting as nutrient carriers for crops. The marine diatom *Halamphora subturgida* was employed for the first time to synthesize INPs and evaluate their application as a nanophycofertilizer (NPF) for rice (*Oryza sativa* L.). The diatom facilitated both intra- and extracellular formation of spindle-shaped nanoparticles (70–100 nm) as confirmed by UV–Vis, DLS, TEM, SEM-EDAX, FTIR, and fluorescence analyses. Biochemical profiling revealed dynamic metabolic shifts during nanoparticle synthesis, with transient increases in pigments, proteins, and lipids followed by their decline, while iron and carbon content rose steadily. Antioxidant enzyme assays indicated early oxidative stress followed by metabolic adaptation, underscoring the diatom's resilience as a biofactory. When applied to rice seedlings, the INP-loaded diatoms significantly outperformed diatoms or nanoparticles alone, increasing shoot length by approximately 45%, root length by 50%, fresh biomass by 18%, chlorophyll content by 42%, iron accumulation by nearly twofold, and silica uptake by about 43% compared with the untreated control. These synergistic effects highlight the dual role of diatoms as both stabilizers and nutrient carriers, delivering iron in a highly bioavailable form while simultaneously contributing silica for structural strength. The findings position diatom-mediated nanofertilizers as sustainable alternatives to chemical fertilizers, offering a multifaceted strategy to boost crop vigor, nutrient density, and early-stage resilience in rice.

Keywords: Iron nanoparticles; Diatoms; Green nanotechnology; Rice; Sustainable agriculture

1. Introduction

Rice (*Oryza sativa* L.) is a staple food crop for nearly half of the world's population, and its production is crucial for global food security [1,2]. However, conventional agricultural practices rely heavily on chemical fertilizers, which pose environmental risks, including soil degradation, water pollution, and greenhouse gas emissions [3,4]. Sustainable and eco-friendly alternatives are being explored to address these challenges, including bio-based nanofertilizers that enhance nutrient availability and plant growth. Iron (Fe) is an essential micronutrient for plant development, playing a vital role in chlorophyll biosynthesis, respiration, and enzyme functions [5,6]. Iron deficiency in rice seedlings leads to reduced growth, lower

chlorophyll content, and diminished photosynthetic efficiency. Traditional iron fertilizers, such as $FeSO_4$, suffer from low bioavailability due to rapid oxidation and precipitation in soil [7]. Nanotechnology-based fertilizers, particularly INP, have shown promise in improving iron uptake efficiency and promoting plant health [8,9].

Algae-mediated nanoparticle synthesis has attracted considerable attention as an eco-friendly and cost-effective approach [10,11]. Green algae (*Ulva*) and cyanobacteria (*Spirulina*) have previously been used to synthesize INP for nano-phycofertilizer (NPF) applications [12,13]. In contrast, diatoms, with their silica-rich frustules, offer the additional advantage of serving as natural nanoparticle carriers while supplying bioavailable silica, an essential beneficial element for rice [14]. *Halamphora subturgida*, a marine diatom with high surface area and bioactive compounds, therefore represents a promising platform for INP synthesis. Silica from diatom frustules enhances plant structural integrity, photosynthetic efficiency, and tolerance to biotic and abiotic stresses [15–17]. The combined availability of INP and silica may thus synergistically promote rice seedling growth.

In this study, *Halamphora subturgida* was employed to synthesize INP, which were characterized using light microscopy, UV–Vis spectroscopy, DLS, SEM-EDAX, TEM, FTIR, and fluorescence analyses. The physiological and biochemical responses of the diatom during nanoparticle synthesis were also investigated. Finally, the growth-promoting potential of INP-loaded diatoms was evaluated in rice seedlings by comparing control, diatom, INP, and NPF treatments. This study demonstrates the potential of *H. subturgida* as both a nanoiron biofactory and a silica-rich nutrient carrier for enhancing early rice seedling growth (Figure 1).

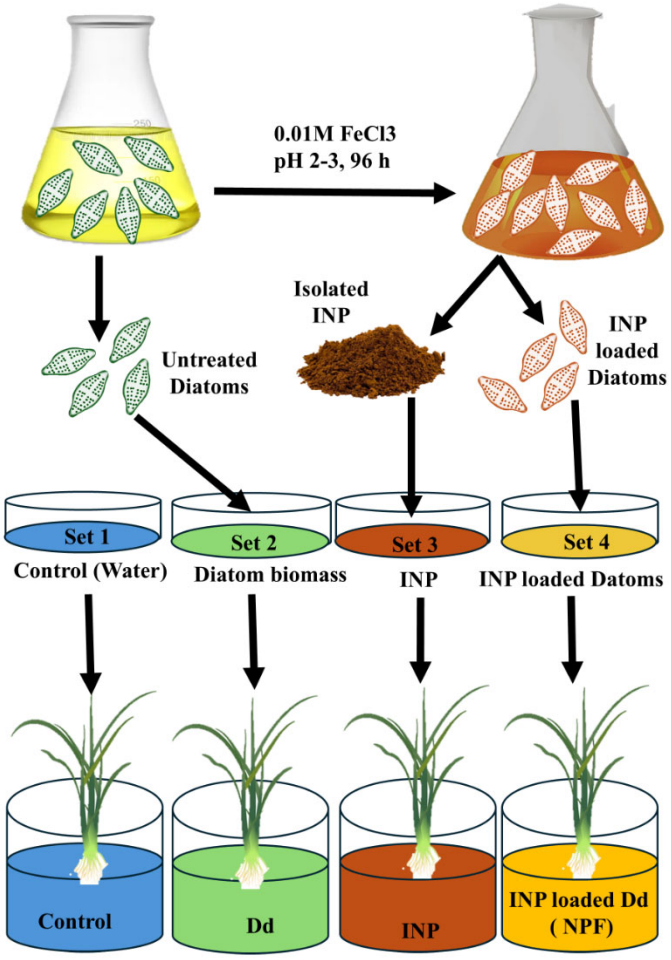

Figure 1. The schema of the work.

2. Materials and Methods

2.1. Culture Maintenance and Production of Iron Nanoparticles

The diatom strain *Halamphora subturgida* was obtained from the Calcutta University Herbarium and Algal Culture Collection Unit and maintained in diatom-specific culture medium under controlled laboratory conditions. The culture was grown under a photoperiod of 16:8 h light-dark cycle at a temperature of 25 ± 2 °C with continuous aeration to ensure optimal growth. The medium was periodically replenished to maintain the health and stability of the diatom population prior to use in INP synthesis. For the synthesis of INPs, *Halamphora subturgida* cultures were exposed to different concentrations of the iron precursor salts ($FeCl_3$) (0.001 to 0.01) and pH (1 to 6) conditions to determine the optimal parameters for nanoparticle formation. The cultures were incubated under sterile conditions with continuous agitation to facilitate nanoparticle synthesis. After 96 h of incubation, a distinct color change in the solution was observed, indicating the successful formation of INPs. The synthesized INPs were separated by adding Sodium citrate and centrifugation at 14,000 rpm for 15 min, followed by repeated washing with deionized water to remove any unreacted iron precursor salts. The purified INP-loaded diatom biomass was then dried and dusted for the application in rice seedling experiments.

2.2. Characterization of Nano-Iron

To confirm the successful synthesis of INPs and analyze their structural, optical, and morphological properties, multiple characterization techniques were employed. These included light microscopy, UV-Vis spectroscopy, scanning electron microscopy (SEM-EDAX), and dynamic light scattering (DLS) analysis.

2.2.1. Light Microscopy

Morphological changes in the diatom biomass following INP synthesis were examined using light microscopy (Carl Zeiss Microscope with Camera attachment). Slides were prepared by placing algal biomass from different experimental setups on clean glass slides, mounting them in 10% glycerol, and covering them with a glass coverslip. The prepared slides were then observed under the microscope, and any structural alterations or aggregations associated with nanoparticle formation were documented.

2.2.2. UV-Vis Spectroscopy

UV-Visible spectroscopy was performed to analyze the surface plasmon resonance (SPR) phenomenon, which is indicative of INP formation due to the oscillation of conduction electrons in the Fe nanoparticles. Approximately 100 mg of treated algal biomass was homogenized in 1 mL of 7.5 mM sodium citrate solution to stabilize the nanoparticles. The sample was then sonicated for 15 min to enhance nanoparticle dispersion. After sonication, the suspension was centrifuged at 9500 rpm for 20 min, and the resulting supernatant was collected for UV-Vis spectroscopic analysis. For extracellular nanoparticle synthesis, the reaction medium was directly mixed with 7.5 mM sodium citrate solution and analyzed. The spectral analysis was performed within the wavelength range of 200–800 nm, and characteristic absorption peaks associated with INPs were recorded.

2.2.3. Scanning Electron Microscopy (SEM) Analysis

The surface morphology and elemental composition of the synthesized INP were examined using SEM with energy dispersive X-ray analysis (EDAX) (Carl Zeiss EVO 18 SEM, Germany). A small amount of INP-loaded diatom biomass was carefully placed onto a glass coverslip. Excess moisture was removed using blotting paper, and the thin film of the sample was allowed to air-dry completely. To enhance conductivity and imaging resolution, the sample was sputter-coated with gold prior to SEM observation.

The SEM micrographs provided insight into the morphology, distribution, and surface interactions of INP within the diatom matrix. Additionally, EDAX analysis confirmed the presence of Fe and other elemental compositions in the treated biomass.

2.2.4. Dynamic Light Scattering (DLS) Analysis

The size distribution and stability of the synthesized INP were analyzed using DLS (Malvern Zetasizer, UK). DLS provides insights into the hydrodynamic diameter and zeta potential, which indicate the stability of nanoparticle dispersion. The INPs (both extracellular and intracellular) were suspended in deionized water and sonicated for 10 min to prevent aggregation. The solution was filtered through a 0.22 µm membrane filter before DLS measurement. The hydrodynamic diameter and polydispersity index (PDI) were recorded to evaluate size uniformity and stability. DLS analysis confirmed the mean particle size distribution and provided valuable information regarding nanoparticle agglomeration and surface charge, which are critical for bioavailability and uptake in plants.

2.2.5. High-Resolution Transmission Electron Microscopy (TEM) Analysis

TEM (JEOL JEM 2100 HR-TEM, Japan) was employed to study particle morphology at an accelerating voltage of 80 keV after applying a 2 µL drop of a nanosuspension with a concentration of 0.05 $mg \cdot mL^{-1}$. The atomic composition of the nanoparticle suspensions was determined using the JEOL JEM 2100 HR-TEM, which was equipped with an EDX detector.

2.2.6. Fourier Transform Infrared (FTIR) Analysis

FTIR analyses were conducted within the spectral range of 400–4000 cm^{-1} to identify the functional groups present on the surface of nanosiliceous frustules and iron-treated frustules. A sample of 2–3 mg of the dried material was combined with approximately 100 mg of oven-dried potassium bromide (KBr) and ground into a fine powder. Subsequently, the powder was compressed under hydraulic pressure for three minutes to form a transparent pellet. This pellet was then mounted on an FT-IR sample holder and analyzed using a Jasco FT/IR-6300 Fourier Transform Infrared Spectrometer, equipped with an IRT-7000 Intron Infrared Microscope (JASCO, Tokyo, Japan).

2.2.7. Fluorescence Study

The fluorescence characteristics of INP-impregnated diatom frustules were examined using confocal laser scanning microscopy (CLSM). The resulting nanohybrids, consisting solely of nanoparticles, were dried for 5 min and subsequently analyzed via fluorescence microscopy. Autofluorescence of the particles under membrane-enclosed, *in vivo* conditions was observed in treated frustules using fluorescence microscopy with a blue filter (λex-425 nm, λem-475 nm) and a red filter (λex-570 nm, λem-670 nm) in the CLSM (Olympus IX 81, Olympus, Tokyo, Japan) equipped with FV-1000 software version 5.8.2. Images were captured using a 40× objective lens.

2.3. Study of Biochemical Changes in Algal Biomass

2.3.1. Estimation of Chlorophyll

Algal tissue (0.5 g) was homogenized in a mortar and pestle using 80% acetone until the tissue became colorless. The total volume of the extract was measured, and the homogenate was centrifuged at 10,000 rpm for 10 min. The supernatant was collected, and its absorbance was recorded at 645 nm and 663 nm using a spectrophotometer. The chlorophyll content was calculated using the following equations: Chlorophyll a (mg/g tissue) = $12.7(A_{663}) - 2.69(A_{645}) \times V/(1000 \times W)$, Chlorophyll b (mg/g tissue) =

22.9(A_{645}) − 4.68(A_{663}) × V/(1000 × W), and Total chlorophyll (mg/g tissue) = [20.2(A_{645}) + 8.02(A_{663})] × V/(1000 × W). Here, A represents absorbance at the respective wavelengths, V is the final volume of the extract in 80% acetone, and W is the fresh weight of the algal biomass [18].

2.3.2. Estimation of Carotenoids

Carotenoid extraction was carried out by homogenizing 0.5 g of algal biomass in acetone followed by centrifugation at 5000 rpm for 10 min. The supernatant was stored overnight at 4 °C in the dark. The extract was vacuum-dried at room temperature and then re-dissolved in equal volumes of petroleum ether and aqueous methanol. For saponification, the crude pigment extract was evaporated to dryness, diluted with water containing 2.5% NaCl, and extracted using petroleum ether in a separating funnel. The upper ether phase containing carotenoids was collected, washed with water, dried over anhydrous sodium sulfate, and filtered. The purified ether extract was concentrated using a rotary evaporator, transferred to a 25 mL conical flask, and dried under nitrogen. The absorbance was measured at 450 nm, and total carotenoid content was calculated using the formula: *Carotenoid* (mg/g) = (D × V × F × 10)/(2500 × W), where D is the absorbance at 450 nm, V is the sample volume, F is the dilution factor, and W is the algal biomass weight [19].

2.3.3. Estimation of Total Carbohydrates

Total carbohydrate content was estimated using the DuBois method [13]. The algal sample was weighed and hydrolyzed in boiling water (90 °C) with 2 mL of 2.5N HCl for 3 h. The hydrolysate was neutralized using sodium carbonate (Na_2CO_3) and incubated for 1 h. The sample was centrifuged at 9500 rpm for 15 min, and 1 mL of the supernatant was mixed with 0.5 mL of phenol and 5 mL of concentrated sulfuric acid (96% H_2SO_4). The reaction mixture was incubated at 25–30 °C for 20 min, and the optical density (OD) was measured at 490 nm to determine the carbohydrate concentration.

2.3.4. Estimation of Total Protein

Protein estimation was performed following the Lowry [13] method. Algal biomass (0.5 g) was homogenized, and the extract was centrifuged to collect the supernatant. To 1 mL of the supernatant, 5 mL of alkaline copper solution (prepared by mixing 49 mL of 2% sodium carbonate in 0.1N NaOH with 1 mL of 0.5% copper sulfate in 1% potassium sodium tartrate) was added and incubated at room temperature for 10 min. Folin-Ciocalteu reagent (0.5 mL) was then added, and the mixture was incubated for 30 min in the dark. The absorbance was measured at 660 nm.

2.3.5. Estimation of Lipid Content

Lipid extraction was carried out by harvesting the algal biomass via centrifugation at 10,000 rpm for 10 min. The biomass was dried in a hot air oven at 60 °C for 2–3 h, then scraped using a sterile scalpel and transferred into a pre-weighed vial. Lipids were extracted using a solvent mixture of chloroform, methanol, and distilled water (2:2:1 ratio). The vial was vortexed for 20 min and then left undisturbed for 2 h to allow phase separation. The lower organic phase containing lipids was filtered using Whatman filter paper, and lipid content was quantified gravimetrically after solvent evaporation [20].

2.3.6. Total Carbon Content Estimation

Carbon content in the rice plants was estimated following the method described by Walkley and Black [21] with slight modifications. Dried plant samples (shoot and root) were finely ground and subjected to digestion using potassium dichromate ($K_2Cr_2O_7$) in an acidic medium. The reaction was carried out in a fume hood by adding 1 g of dried plant to 10 mL of 1 N $K_2Cr_2O_7$, followed by the slow addition of 20 mL of concentrated sulfuric acid (H_2SO_4). The mixture was allowed to cool before titration with ferrous

ammonium sulfate (FAS) solution using diphenylamine as an indicator. The carbon content was calculated based on the reduction of dichromate, and results were expressed as a percentage of total plant dry weight.

2.3.7. Total Iron Content Determination

For total iron content determination, the dry biomass was ground into a fine powder, and 0.5 g of the sample was digested in a mixture of nitric acid (HNO_3) and hydrofluoric acid (HF) (1:2 ratio) using a microwave digestion system (MILESTONE, Lab Tech, Bergamo, Italy) for 24 h. The digested samples were evaporated at 210 °C until the solution was reduced to 1 mL, diluted with ultrapure water, and total iron content was quantified using Inductively Coupled Plasma Optical Emission Spectrometry (ICP-OES; ICAP 630, Thermo Scientific, Waltham, MA, USA) [22].

2.4. Enzymatic Assay in Algal Biomass

2.4.1. Determination of Total Glutathione Content

Algal tissue was homogenized in ice-cold phosphate buffer (pH 7.0), followed by centrifugation at 10,000 rpm for 15 min. The resulting supernatant was collected, and 1 mL was mixed with 0.5 mL of 10 mM DNTB and 3 mL of phosphate buffer. The reaction mixture was thoroughly mixed and incubated at room temperature in the dark for 20 min. A blank was prepared using 0.5 mL of 10 mM DNTB in 4 mL of phosphate buffer. The optical density (OD) was measured at 412 nm, and the total glutathione content was determined from a standard curve and expressed in mg/g tissue [23].

2.4.2. Determination of Lipid Peroxidation Activity

Algal biomass (0.5 g) was homogenized in 5 mL of 0.1% TCA using a mortar and pestle. The homogenate was centrifuged at 10,000 rpm for 20 min, and the supernatant was collected. A volume of 400 µL of the homogenate was mixed with 4 mL of 0.5% TBA and incubated in a water bath at 90 °C for 30 min. The reaction tubes were then cooled, and the solution was centrifuged at 10,000 rpm for 15 min. Absorbance was measured at 532 nm, corrected at 600 nm, and lipid peroxidation levels were determined using the extinction coefficient of MDA (155 $mM^{-1} \cdot cm^{-1}$). The amount of MDA was expressed as µM/g fresh weight of biomass [24].

2.4.3. Determination of Ascorbate Peroxidase Activity

Algal biomass (0.5 g) was homogenized in 0.1 M phosphate buffer (pH 7.0) and centrifuged at 13,000 rpm. The supernatant was mixed with 20 mM phosphate buffer, 4 mM ascorbate, 20 mM H_2O_2, and distilled water. The decrease in ascorbate peroxidase activity was measured at 290 nm using an extinction coefficient of 2800 $M^{-1} \cdot cm^{-1}$. Ascorbate peroxidase activity was calculated using the formula:

$$\text{APX activity} = (\Delta\text{O.D.} \times \text{V} \times 10^6 \times 60)/2800$$

where V represents the volume of the supernatant, and ΔO.D. is the decrease in optical density. The results were expressed as µmol/min/mg protein [25].

2.4.4. Determination of Superoxide Dismutase Activity

0.5 g of Algal biomass was homogenized in 0.2 M sodium phosphate buffer (pH 7.8) at 1–4 °C and centrifuged at 10,000 rpm for 15 min at 4 °C. The supernatant was collected and maintained under cold conditions. The reaction mixture was prepared by sequentially adding 750 µL of phosphate buffer (1 M, pH 7.8), 390 µL of methionine, 300 µL of EDTA, 500 µL of sample, 800 µL of distilled water, 250 µL of NBT, and 6 µL of riboflavin. One set of reaction mixtures was incubated in the dark, while another was exposed to a 15 W light chamber for 10–15 min. A blank was prepared by replacing the sample with

distilled water. Absorbance was measured at 560 nm, and enzyme activity was expressed as mg SOD producing 50% inhibition per g protein.

The percentage inhibition of SOD activity was calculated using the formula:

$$A\% = [(X - Y) \times 8 \times 100]$$

where X is the OD value of the light-exposed blank, and Y is the OD value of the light-exposed reaction mixture. The enzyme activity corresponding to 50% inhibition was determined using:

$$50\% \text{ inhibition of SOD activity} = (C \times 50)/(B \times A)$$

where C is the total protein concentration, B is the reaction volume, and A is the inhibition percentage [26].

2.4.5. Determination of Catalase Activity

Algal biomass was homogenized in 0.05 M phosphate buffer (pH 7.0) at 1–4 °C and centrifuged at 10,000 rpm for 15 min at 4 °C. The supernatant was collected, and hydrogen peroxide-phosphate buffer was prepared by diluting 0.05 mL of 30% *(w/v)* H_2O_2 to 100 mL with phosphate buffer. A reaction mixture containing 2.9 mL of H_2O_2-phosphate buffer and 0.1 mL of enzyme extract was prepared, and the decrease in OD was measured at 240 nm. A blank containing only phosphate buffer was used as a reference. The time required for the OD to decrease from 0.45 to 0.04 was recorded, and catalase activity was calculated using the formula:

$$\text{Catalase activity} = (\Delta O.D. \times V \times 10^6 \times 60)/(39.4 \times t)$$

where V represents the volume of enzyme extract, and t is the reaction time. The enzyme activity was expressed in µmol/min [27].

2.5. Application of Iron Nanoparticle-Loaded Diatoms in Rice Plants

Rice seeds (*Oryza sativa* L. var. Khitish) were obtained from the Rice Research Station, Chinsurah, Government of West Bengal, India. Prior to experimentation, the seeds were surface-sterilized by sequentially washing with 50% ethanol for 5 min, treating with 2% sodium hypochlorite (NaOCl) for 5 min, and then rinsing thoroughly with sterile distilled water to remove any residual chemicals.

To evaluate the efficacy of INP-loaded diatom dust (Set 4: INP-loaded Dd) in enhancing seedling growth, a comparative analysis was conducted across four experimental conditions. The first set served as the untreated control without any additional treatment (Set 1: Control). The second set consisted of diatoms alone (Set 2: Dd), while the third set included only INP (Set 3: INP). The fourth set comprised diatoms loaded with INP, representing the NPF treatment. This comparative approach was employed to determine whether the synergistic interaction between INP and diatoms could exert a greater stimulatory effect on rice seedling growth compared to the individual components. All the sets were prepared in Yoshida solution. The optimal concentration of INP, as determined from previous studies, was standardized at 0.2% for subsequent application of rice plant growth. The amounts of NPF and algal biomass (Diatom dust or Dd) used in the experiments were also determined based on the INP content within the algal matrix. The NPF and ABM application rates were adjusted to match the iron content delivered by the INP treatment, ensuring consistency across experimental conditions.

Six rice seedlings were maintained in each set, and plant growth parameters were monitored at 30 days after germination. Measurements included shoot length, root length, chlorophyll content, fresh biomass, leaf number, and leaf length. Additionally, iron content and silica content in plant tissues were quantified using Inductively Coupled Plasma Optical Emission Spectroscopy (ICP-OES).

2.6. Preparation of Graphs and Statistical Analysis

All experiments were conducted in triplicate to ensure data reliability and reproducibility. The graphical representations, including bar charts depicting mean values with standard deviation error bars, were created using GraphPad Prism 8.4.3. Statistical significance was evaluated using an Ordinary one-way ANOVA, followed by Tukey's multiple comparisons test to determine differences between treatment groups. A significance level of $p < 0.05$ was considered statistically meaningful. In the graphical presentation of the results, different levels of significance are represented as $p \leq 0.05$ (*), $p \leq 0.01$ (**), $p \leq 0.001$ (***), and $p \leq 0.0001$ (****), whereas "ns" indicates a non-significant difference.

3. Results

3.1. INP Synthesis

The biosynthesis of INP was carried out using a 0.01 M $FeCl_3$ solution under controlled conditions, with the pH maintained at 2–3. The reaction was allowed to proceed for 96 h, during which a distinct color change was observed, indicating successful nanoparticle formation. Initially, the algal biomass exhibited a fresh green color, which gradually shifted to a golden brown hue, suggesting both intracellular and extracellular synthesis of INP. The intracellular formation was evident from the pigmentation retained within the cells, whereas extracellular synthesis was inferred from the color transformation in the surrounding medium (Figure 2). The ability of this diatom species to facilitate both intra- and extracellular nanoparticle formation highlights its unique biochemical potential. This study presents the first report of *Halamphora subturgida* mediating the synthesis of INP.

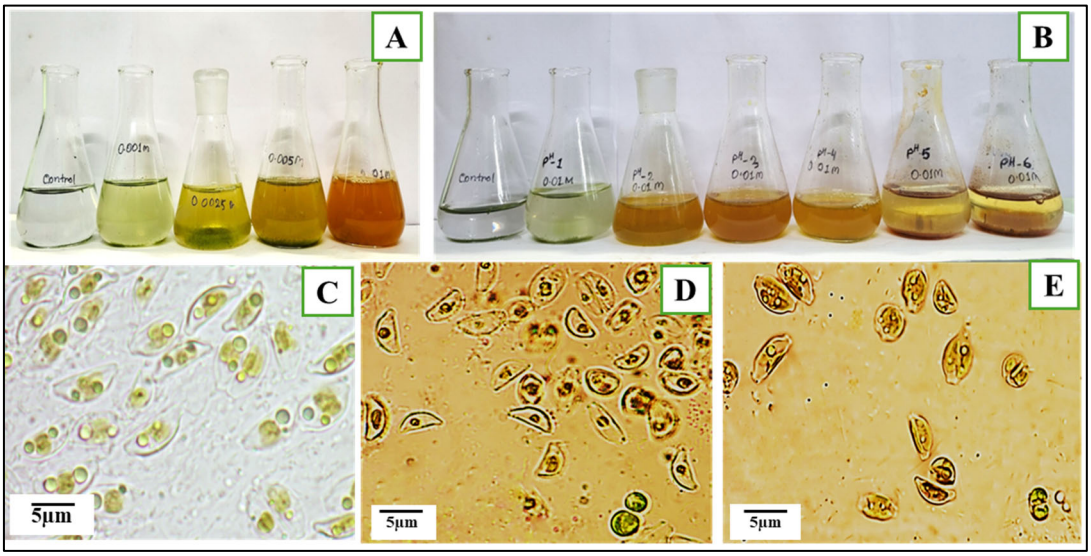

Figure 2. Change in Diatom during INP production. (**A**) Exposure in different precursor salt concentration; (**B**) Exposure in different pH; (**C**) Microscopic image of *Halamphora subturgida* (100×) without any treatment; (**D**,**E**) *Halamphora subturgida* cells after INP production (100×).

3.2. Characterization of Synthesized INPs

3.2.1. Morphological Changes

The morphological changes in *Halamphora subturgida* during INP synthesis were observed under a light microscope (100× magnification) over a 96-h exposure period. Initially, during the first six hours, no significant alterations were detected in the algal cells, indicating that the early stages of incubation did not induce visible stress or transformation. However, by 12 h, a gradual reduction in cell size and changes in cell shape became evident, suggesting an early physiological response to $FeCl_3$ exposure. As the exposure

progressed to 24 h, the formation of resting spores was observed, accompanied by a further decrease in cell size. By 48 h, the outer surfaces of the cells began to turn slightly brown, and cell aggregation became prominent, indicating possible nanoparticle interaction with the algal surface. Resting spore formation continued, signifying a stress-induced survival mechanism. At 72 h, extracellular deposition of nanoparticles commenced, with a majority of cells converting into resting spores. Aggregation intensified, and some cells exhibited protoplasmic disintegration, suggesting increased nanoparticle interactions and potential intracellular release. Additionally, spore shape distortion was noted, further supporting the hypothesis of nanoparticle-induced stress responses. By 96 h, the algal surface exhibited a pronounced brown coloration, and extracellular nanoparticle deposition became more prominent. Nearly all cells were clumped together, highlighting extensive nanoparticle synthesis and accumulation. These observations suggest that *Halamphora subturgida* not only acts as a biological matrix for nanoparticle formation but also undergoes significant physiological and morphological adaptations in response to iron exposure. The progressive changes in cell structure and nanoparticle deposition confirm the dynamic role of this diatom in nanoparticle biosynthesis, further establishing its potential as a natural bio-factory for sustainable nanomaterial production.

3.2.2. UV-Spectroscopy

The biosynthesis of INP by *Halamphora subturgida* was further confirmed through UV-Visible spectroscopy (Figure 3A). The spectral analysis revealed a distinct absorbance peak at 230 nm, indicating the presence of INP in the reaction mixture. This characteristic peak corresponds to the surface plasmon resonance (SPR) of Fe nanoparticles, which is influenced by particle size, shape, and surrounding medium. The appearance of this peak suggests efficient nanoparticle formation and stabilization within the algal system. The observed peak at 230 nm aligns with previously reported values for Fe(III) and Fe(0) nanoparticles, confirming the reduction of Fe^{3+} ions to nano-sized iron particles. The shift in absorbance, compared to standard $FeCl_3$ solutions, also indicates successful biotransformation facilitated by the diatom. The increase in absorbance intensity over time further supports progressive nanoparticle accumulation and extracellular deposition, as observed in the light microscopy study.

3.2.3. DLS Analysis

The hydrodynamic size distribution of the biogenic INPs synthesized by *Halamphora subturgida* was analyzed using DLS (Figure 3B). The average hydrodynamic diameter of the synthesized INPs was found to be 132.3 nm, with a polydispersity index (PDI) of 0.394. The relatively low PDI value suggests a moderately uniform size distribution, indicating the nanoparticles are well-dispersed in the solution with minimal aggregation. The size distribution histogram shows that the majority of the nanoparticles fall within the 10–100 nm range, with a peak around 30 nm, which suggests that a significant fraction of the synthesized particles are in the nanoscale range. However, the presence of some larger aggregates likely contributed to the slightly higher average hydrodynamic diameter.

3.2.4. EDX Analysis

The Energy Dispersive X-ray (EDX) spectrum confirmed the presence of iron (Fe) as the primary element in the synthesized nanoparticles (Figure 3C). Distinct iron peaks were detected at 0.7 keV, 1.0 keV, 6.4 keV, and 7.0 keV, which are characteristic signals of iron. The intensity of these peaks indicates a strong iron presence, confirming the successful biosynthesis of INPs by *Halamphora subturgida*. The high signal strength of iron in the spectrum suggests efficient nanoparticle formation with minimal interference from other elements.

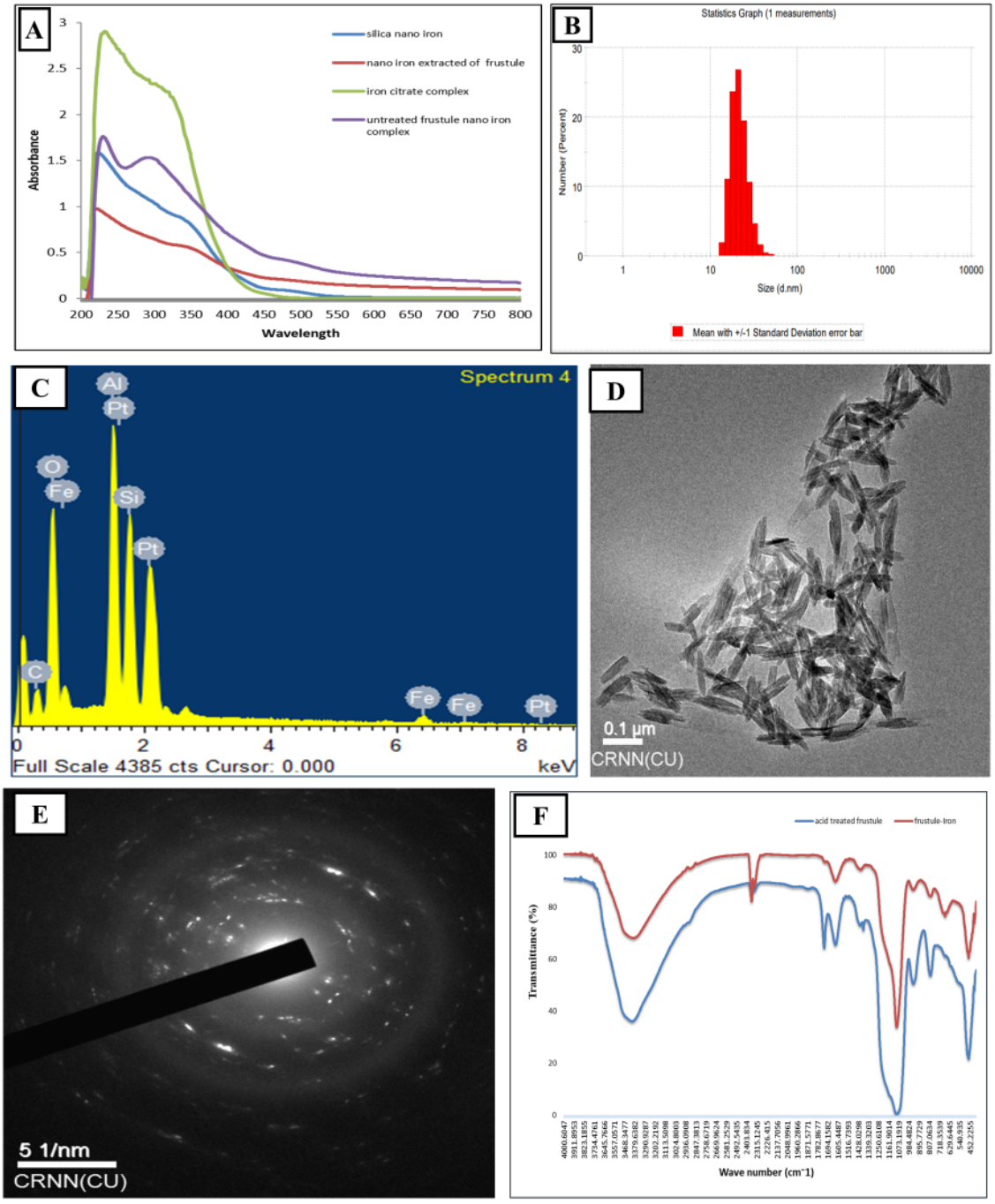

Figure 3. Characterization of the produced INPs. (**A**) UV Spectroscopy, (**B**) DLS analysis, (**C**) EDAX analysis, (**D**) TEM analysis, (**E**) SAED analysis, (**F**) FTIR analysis.

3.2.5. TEM and SAED Analysis

The TEM observations provide a definitive depiction of the morphology and dimensions of the INPs produced by the experimental taxa (Figure 3D). The TEM analysis confirmed that all synthesized particles, both extracted and extracellular, exhibit a spindle shape with nearly uniform size. The average length of the nano-spindles ranged from 70 to 100 nm, while the width varied between 20 and 30 nm. The SAED (Selected Area Electron Diffraction) pattern of the synthesized INP exhibited well-defined concentric diffraction rings and scattered bright spots, confirming its polycrystalline nature. The presence of multiple rings indicates the crystalline arrangement of iron within the nanoparticles, while the spotty distribution along the rings suggests the existence of nanocrystals with different orientations. These diffraction features

provide strong evidence that the diatom-mediated synthesis yielded INP with good crystallinity rather than amorphous structures (Figure 3E).

3.2.6. FTIR Analysis

The surface-coating biomolecules of the stabilized nanohybrid structures were identified through FT-IR analyses, in comparison to their nanostructured biosilica precursor (Figure 3F). In both acid-treated and silver-treated frustules, the presence of siloxane and silane groups was confirmed by a peak observed between 1250 and 950 cm^{-1}. A broad Si–O peak was detected at 1055 cm^{-1}, with an additional peak around 1200 cm^{-1}. The bands at approximately 1060 and 843 cm^{-1}, attributed to Si–O vibrations, were present in both the nanoporous silica and SiO_2–Fe nanostructures. The C–H bonds appeared weakly due to the presence of hydrocarbons and lipids at 2924 and 2852 cm^{-1} in siliceous frustules, and these bands remained conserved even after acid hydrolysis. Similar vibrations were absent in the nanohybrid structures. The broad peaks at 3338–3356 cm^{-1} were attributed to the presence of –OH groups of silanol in the biogenic nanosilica of diatoms, whereas the peak was notably flattened in the case of SiO_2–Fe nanostructures. Vibrations originating from approximately 1642 cm^{-1} and 1543 cm^{-1}, corresponding to the amide I and amide II groups, respectively, were observed in the control sample, while the peak was reduced in the conjugate nanohybrids. The amide bands were due to silica-bound proteins and may be responsible for the reduction of Iron (Fe^{2+}) ions to nanoiron.

3.2.7. Fluorescence Study

Frustules treated with iron demonstrated enhanced *in vivo* auto-fluorescence subsequent to the synthesis of nanoiron. This fluorescence was detected in the blue region of the spectrum when excited at 425 nm (Figure 4). A similar outcome was observed when the extracted dry particle pellets were exposed to the same excitation wavelength. The blue fluorescence of the nanoiron micro-aggregations was distinct, and this confirms that it originated exclusively from the nanoparticles. Together, the fluorescence and spectral data validate that diatom frustules serve as efficient scaffolds for INP loading, producing a stable frustule–iron complex suitable for biofertilizer application.

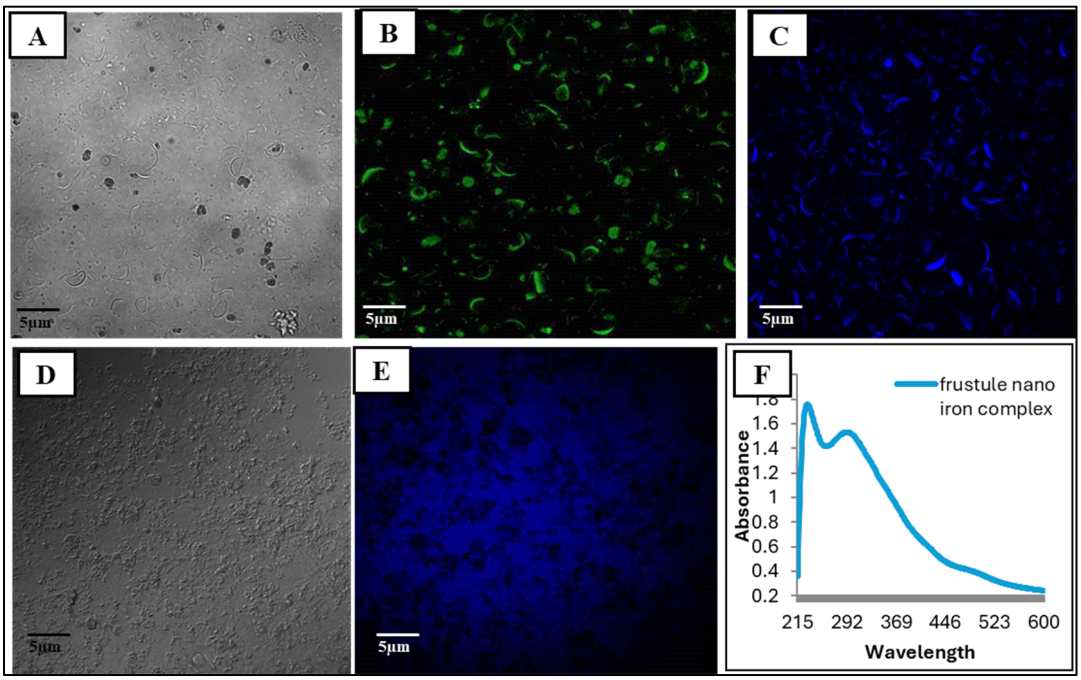

Figure 4. Fluorescence microscopy and absorbance spectra of *Halamphora subturgida* frustules with and without INP loading. (**A**) Bright-field image of untreated frustules. (**B**) Green fluorescence signal indicating silica-rich frustules. (**C**) Blue fluorescence

corresponding to INP deposition on frustules. (**D**,**E**) Control frustules showing minimal background fluorescence. (**F**) UV–Vis absorbance spectrum of the frustule–iron nanoparticle complex, with characteristic peaks confirming nanoparticle incorporation.

The SEM analysis revealed distinct morphological characteristics of the synthesized INPs. The images demonstrated the presence of spindle-shaped structures and nanoflower-like formations, indicating the self-assembly and aggregation of nanoparticles on the diatom surface (Figure 5). At lower magnifications, the diatom frustule structure remained intact, but at higher magnifications, nanoparticle deposition became more prominent. The nanoflower morphology suggests a high surface area, which could enhance interactions with plant roots when applied as a biofertilizer. These observations align with the EDX results, confirming the successful biosynthesis of INP by *Halamphora subturgida*. The presence of well-defined spindle and nanoflower formations indicates that the biogenic synthesis process influenced the nanoparticle morphology, potentially enhancing its bioavailability and functionality in agricultural applications.

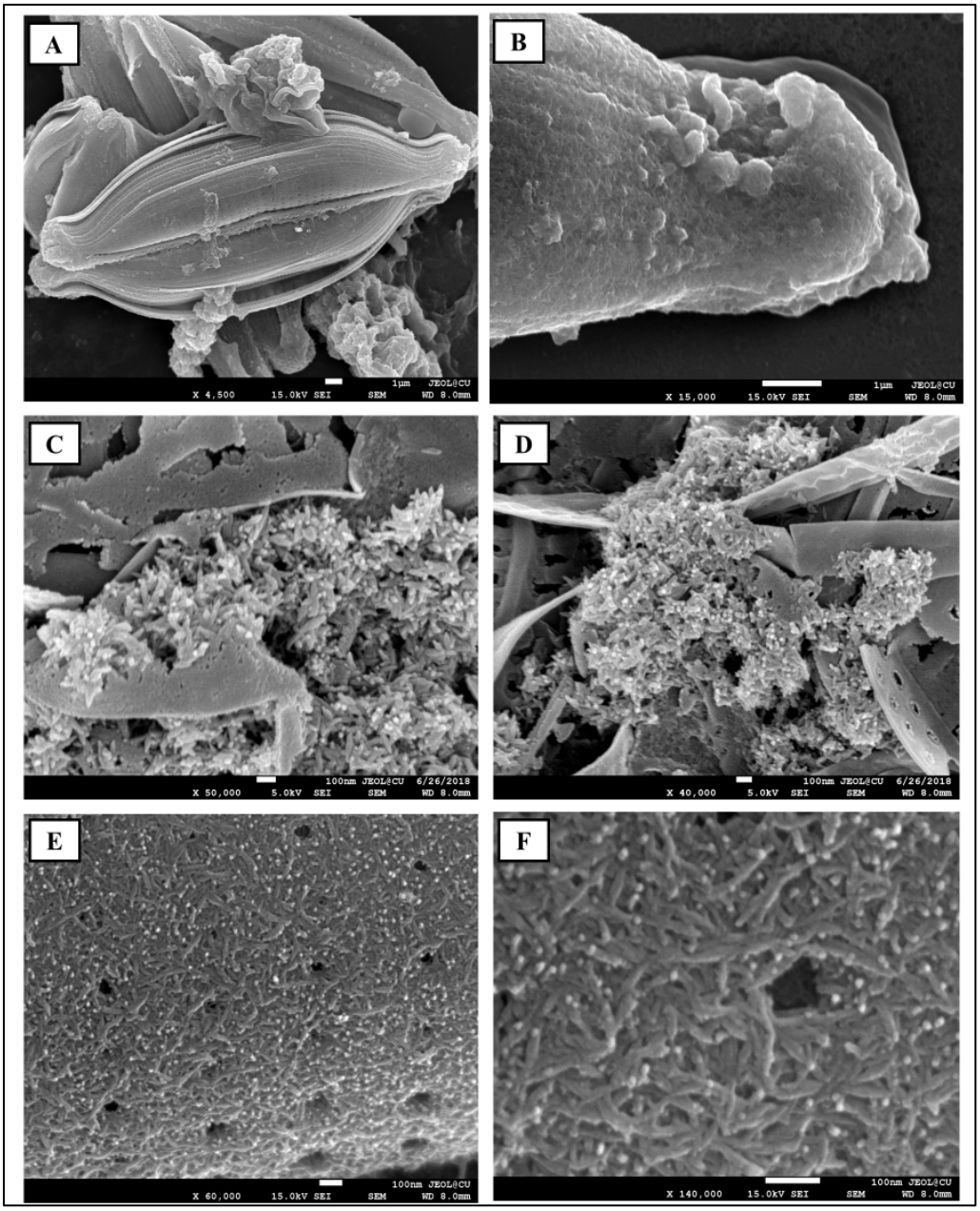

Figure 5. SEM analysis of *Halamphora subturgida* during INP synthesis showing INP deposition on an algal cell. (**A**) Overall deposition pattern of INPs on diatom cell; (**B**) Prominent deposition at the terminal part of diatom cell; (**C**,**D**) Formation of iron nanoparticles on the outer surface of the diatom cell; (**E**,**F**) Presence of spindle-shaped INPs on the diatom cell body.

3.3. The Biochemical Changes in Algal Body During INP Synthesis

The biochemical profile of *Halamphora subturgida* during INP synthesis showed clear temporal variations. Chlorophyll and carotenoids exhibited early stability with a slight increase but declined progressively after prolonged exposure, suggesting oxidative stress–induced pigment degradation (Figure 6A,B). Carbohydrates initially remained stable and peaked around 12 h, indicating a stress-induced accumulation, but later declined steadily, reflecting depletion of energy reserves (Figure 6C). Protein levels followed a biphasic response, with a temporary rebound at 12–24 h, possibly due to stress-mitigating protein synthesis, before dropping sharply at later time points (Figure 6D). Lipids also showed an initial rise, consistent with membrane remodeling and protective compound accumulation, followed by a pronounced decline, likely due to peroxidation and breakdown under oxidative conditions (Figure 6E). In contrast, total carbon content increased consistently throughout the study period, implying active carbon sequestration and structural reinforcement as part of the adaptive strategy (Figure 6F). Notably, iron levels showed a continuous and significant accumulation, exceeding tenfold higher than controls, indicating efficient uptake and stable incorporation into the diatom biomass (Figure 6G). Together, these trends suggest that while diatom metabolism initially adapts to nanoparticle stress through transient upregulation of pigments, carbohydrates, proteins, and lipids, prolonged exposure results in their decline, whereas carbon and iron deposition remain consistently enhanced, underscoring the dual role of *H. subturgida* as both a stress-tolerant biofactory and an efficient nano-iron reservoir.

3.4. Stress-Related Enzyme Assays in Algal Biomass

The antioxidant enzyme profile of *Halamphora subturgida* showed distinct temporal responses during INP synthesis. Superoxide dismutase (SOD) and catalase (CAT) activities rose sharply and peaked at 6 h, reflecting an early response to elevated ROS levels during the active phase of nanoparticle formation, followed by a gradual decline (Figure 6I,L). Peroxidase (POD) activity increased progressively, reaching its maximum at 12 h, suggesting a more sustained role in ROS detoxification (Figure 6J). Ascorbate peroxidase (APX) showed a delayed peak at 24 h, consistent with its function in the ascorbate–glutathione cycle and secondary regulation of oxidative stress (Figure 6K). Glutathione reductase (GR) exhibited a steady increase, with maximum activity at 48 h, indicating prolonged redox balance maintenance and recovery after the initial oxidative burst (Figure 6H). Overall, these patterns indicate that oxidative stress was most pronounced in the early stages of INP formation (6–12 h), as reflected by peaks in SOD, CAT, and POD, whereas APX and GR remained active for longer periods, supporting extended antioxidant defense and stabilization of nanoparticle synthesis.

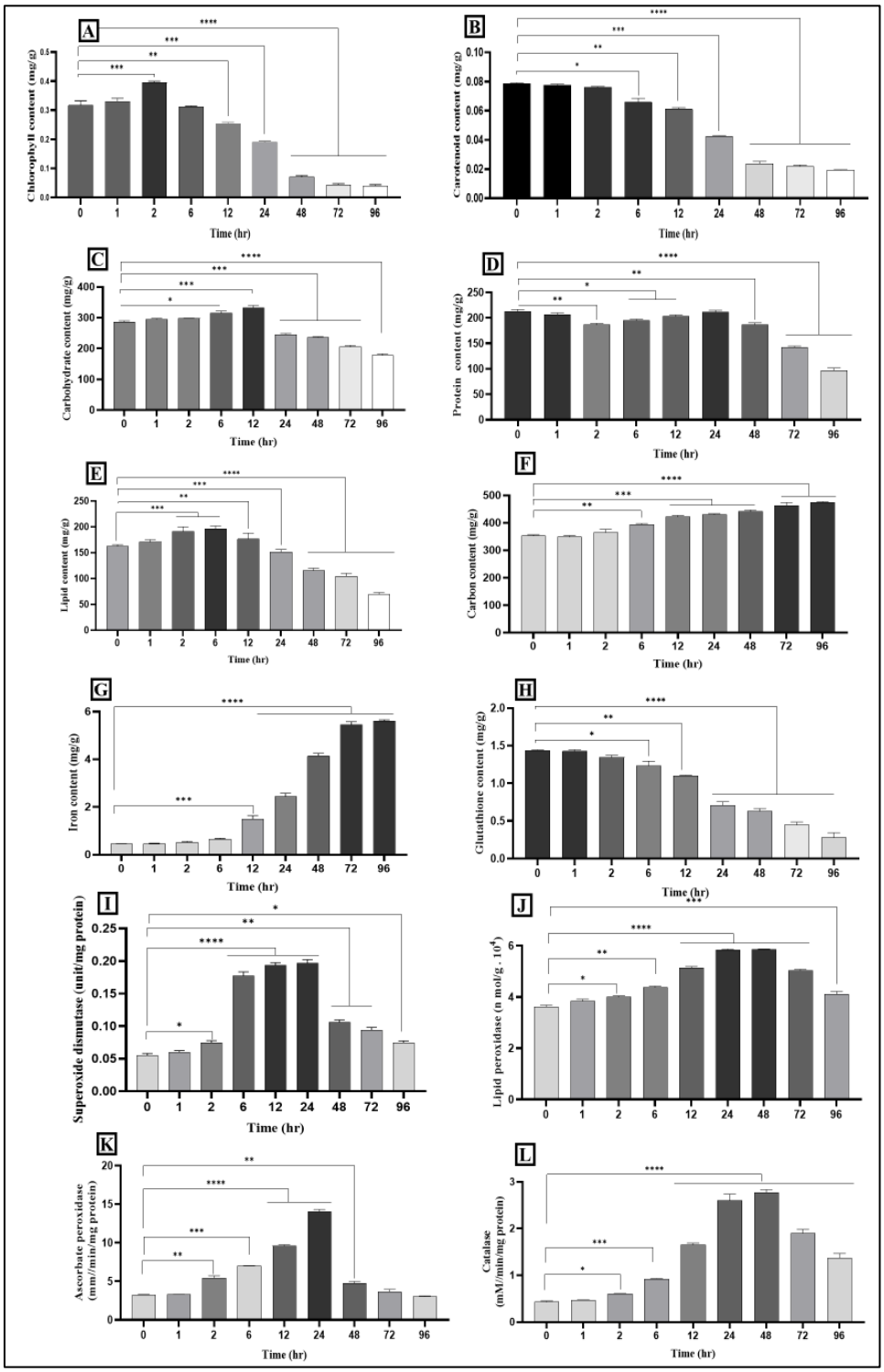

Figure 6. Biochemical and stress-related enzyme assays in algal biomass during INP production. (**A**) Chlorophyll content, (**B**) Carotenoid content, (**C**) Carbohydrate content, (**D**) Protein content, (**E**) Lipid content, (**F**) Carbon content, (**G**) Iron content, (**H**) Glutathione content, (**I**) Superoxide dismutase content, (**J**) Lipid peroxidase content, (**K**) Ascorbate peroxidase content, (**L**) Catalase content. In all histograms, columns represent the average values, while bars represent standard deviations. Stars denote significant differences between control and treated sets; * $p \leq 0.05$, ** $p \leq 0.01$, *** $p \leq 0.001$, **** $p \leq 0.0001$.

3.5. Application of NPF in Rice Seedlings in Hydroponics

As the iron content in the algal biomass (NPF) was quantified using ICP-OES, revealing an iron concentration of 58.41 mg/g, the required amount of NPF as a priming agent was calculated based on the optimized INP concentration of 0.2%. This optimization was determined through previous literature studies,

which identified 0.2% as the most effective concentration for enhancing seedling growth without causing toxicity [12,13]. Consequently, the corresponding amount of NPF was standardized at 3.4% to match the iron content of the INP treatment. Both NPF and untreated algae were applied at 3.4%, whereas the INPs were applied at 0.2%, ensuring that all treatment sets received a fixed amount of iron. This standardization was crucial in eliminating variability due to differences in iron concentration, allowing for a precise comparison of the effects of different iron sources on seed germination and early seedling growth.

The impact of INP-loaded diatoms (NPF) on rice seedling growth showed a consistent pattern of superiority over all other treatments (Figure 7). Shoot elongation was most pronounced in the NPF group, followed by diatoms alone, while INP alone contributed only marginal gains (Figure 8A). A similar trend was observed for root development, where diatoms improved elongation substantially, but the effect was maximized when combined with INPs, suggesting better nutrient absorption and stronger establishment (Figure 8B). Leaf traits reflected the same progression. The number of leaves per seedling increased under diatom treatment, but the addition of INPs further enhanced leaf production and expansion, with NPF consistently supporting the largest and most numerous leaves (Figure 8C,D). Fresh biomass also followed this trend, showing modest improvement under INP alone, stronger effects with diatoms, and the greatest increase under NPF treatment, indicating cumulative benefits of combined nutrient sources (Figure 8E).

Physiological parameters supported these growth observations. Chlorophyll content, a marker of photosynthetic capacity, was elevated in all treatments, with NPF producing the highest levels, followed by INP and then diatoms alone (Figure 8F). Tissue nutrient analysis confirmed these patterns: iron accumulation was significantly enhanced by INPs, but the combination with diatoms resulted in the most efficient uptake, more than doubling relative to untreated plants (Figure 8G). Silica deposition, supplied primarily by the diatom frustules, was also highest in the NPF group, while INP treatment alone slightly reduced silica content compared to the control, suggesting that diatoms facilitated balanced nutrient assimilation (Figure 8H). These results suggest that while diatoms contribute to seedling growth through their bioactive compounds and nutrient availability, their efficacy is significantly enhanced when combined with INPs. The superior performance of the NPF treatment highlights its potential as a sustainable and effective biofertilizer, enhancing iron bioavailability and stimulating growth in early-stage rice seedlings. The sharp rise in iron accumulation suggests enhanced bioavailability and uptake efficiency facilitated by nanoparticle-mediated delivery. The ability of INP-loaded diatoms to significantly enrich iron reserves in plant tissues further underscores their potential as a sustainable biofortification strategy, improving not just growth but also the nutritional profile of crops.

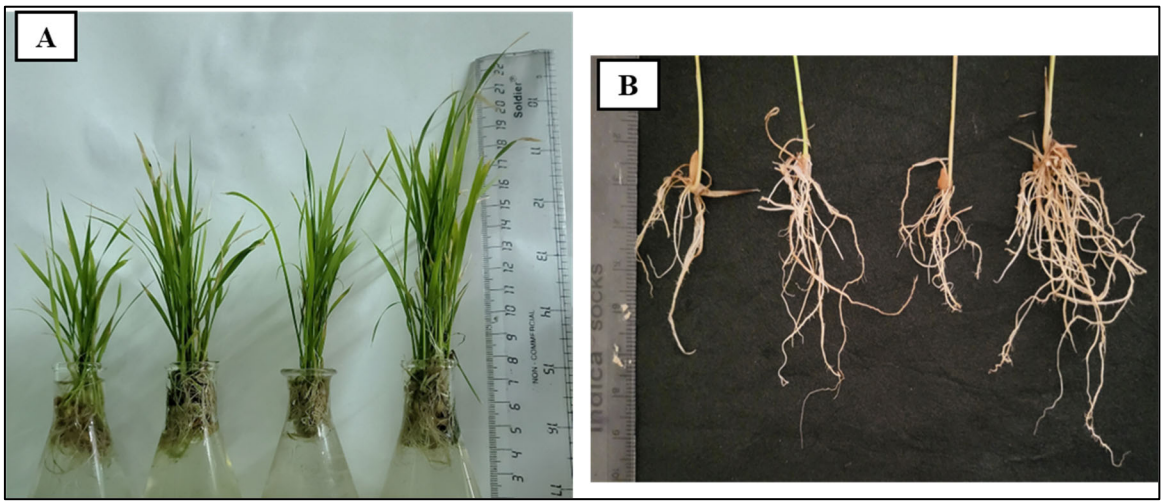

Figure 7. Rice seedling morphology. (**A**) Plant growth with different treatments. From left-hand side control (No treatment), Dd (Algal dust), INP (Iron nanoparticles), Dd loaded algal (NPF) dust. (**B**) Root morphology of rice plants with different treatments, following the same as mentioned above.

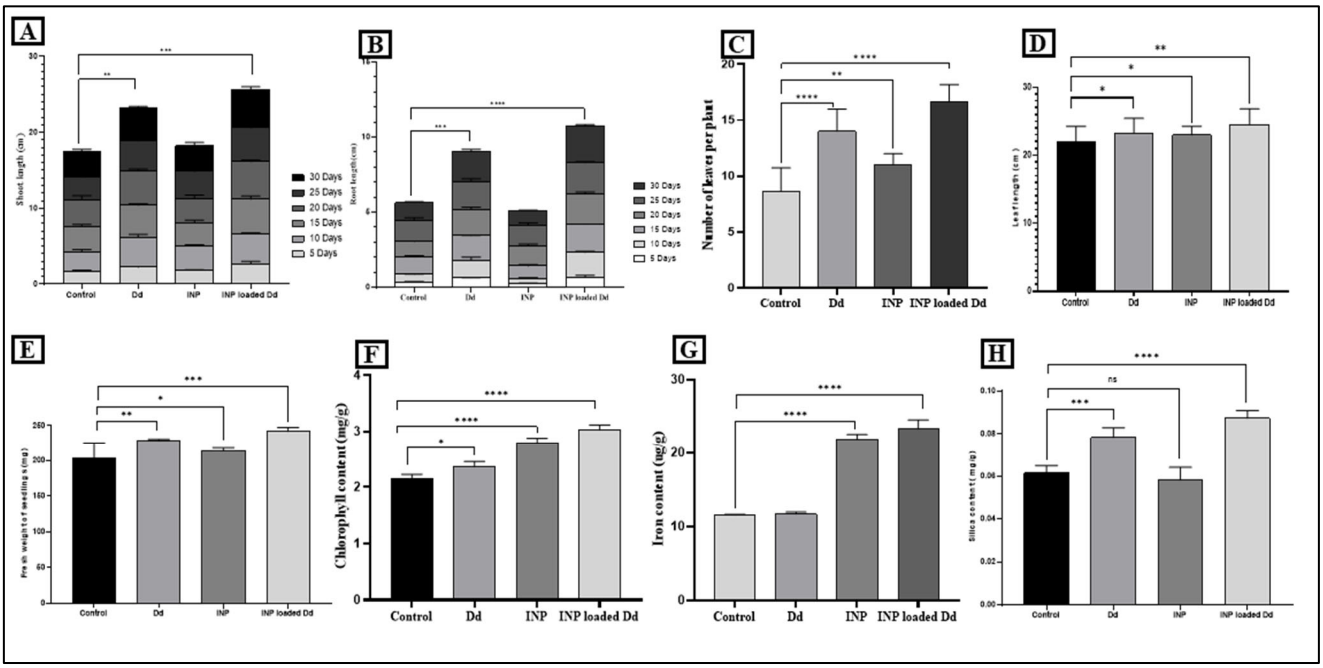

Figure 8. Growth-related parameters in rice seedlings. (**A**) Shoot length, (**B**) Root length, (**C**) Number of leaves per plant, (**D**) Leaf length, (**E**) Fresh weight of the seedlings, (**F**) Chlorophyll content, (**G**) Iron content, (**H**) Silica content. In all histograms, columns represent the average values, while bars represent standard deviations. Stars denote significant differences between control and treated sets; ns: $p > 0.05$, * $p \leq 0.05$, ** $p \leq 0.01$, *** $p \leq 0.001$, **** $p \leq 0.0001$.

4. Discussion

The synthesis of INPs using diatoms presents a novel approach in nanobiotechnology, leveraging the unique properties of these microalgae for environmentally friendly nanoparticle production. This method aligns with the growing interest in green synthesis techniques that utilize biological organisms to fabricate nanoparticles, minimizing the use of hazardous chemicals and reducing environmental impact. In recent years, algae-mediated synthesis of INPs has garnered significant attention for its eco-friendly, cost-effective approach. Algae-mediated synthesis of INPs has emerged as one of the promising eco-friendly approaches, with various algal species demonstrating unique synthesis capabilities [2,28,29]. Studies with *Spirulina platensis* and *Arthrospira platensis* have reported the formation of agglomerated, non-uniform magnetic INPs stabilized over a short period at room temperature [12,30]. Similarly, *Ulva lactuca* extracts have been used to synthesize more uniform, spherical INPs in the 20–40 nm range, highlighting the influence of species-specific biomolecules on nanoparticle morphology [31]. The use of *Chlorella vulgaris* has also resulted in discrete, spherical INPs ranging from 8 to 17 nm, with rapid formation upon interaction with $FeCl_3$ solutions [32]. Meanwhile, brown seaweed *Dictyota dichotoma* facilitated the production of larger, cubic INPs between 40 and 50 nm, suggesting that polysaccharides and secondary metabolites in macroalgae may influence nanoparticle shape [33]. The red seaweed *Kappaphycus alvarezii* has further demonstrated the ability to produce Fe_3O_4 nanoparticles with a mean particle size of 14.7 nm, though aggregation tendencies were observed, likely due to hydroxyl groups in the extract [34]. The biosynthesis of INPs by *Halamphora subturgida* demonstrated distinct morphological and physiological changes in the diatom cells over time. The progressive reduction in cell size, formation of resting spores, and extracellular deposition of nanoparticles align with previous studies on diatom-mediated nanoparticle synthesis.

Nanoparticles show characteristic absorbance maxima in the ultraviolet and visible region of the electromagnetic spectrum due to their surface plasmon resonance property caused by the oscillation of conduction electrons. [35] reported that the UV-Vis spectra of $FeCl_3$ (aqueous) solutions showed well-defined peaks at 220 nm and 290 nm, which corresponded to octahedral $Fe(H_2O)_6^{3+}$ and $Fe(OH)(H_2O)_5^{2+}$

complexes present in aqueous solution of $FeCl_3$. However, after nanoparticle synthesis, the nanoiron suspensions showed new peak positions different from those of bulk iron. Similar peak positions of INP were also found by several reports [12,13,30,36]. Increased nanoparticle concentration caused increased absorption of the suspension, resulting in an intense peak. The hydrodynamic size analysis via DLS revealed an average particle size of 132.3 nm with a polydispersity index (PDI) of 0.394, indicating moderate size uniformity [37]. These results are comparable to those reported by Singh et al. [38], in which biosynthesized INP from Nitzschia palea exhibited a similar size range and minimal aggregation. The presence of nanoparticles predominantly in the 10–100 nm range suggests high bioavailability, making them suitable for agricultural applications [39]. Elemental analysis using EDX confirmed iron as the dominant component in the synthesized nanoparticles, with characteristic Fe peaks at 0.7 keV, 1.0 keV, 6.4 keV, and 7.0 keV. These results are consistent with previous studies on biogenic INP formation by cyanobacteria and diatoms [40]. The high intensity of iron peaks indicates efficient nanoparticle biosynthesis, further supporting the role of diatoms as effective biological platforms for nanomaterial production. SEM imaging provided insights into the morphology of the synthesized INPs, revealing spindle-shaped and nanoflower-like structures. This is in agreement with the work of Patel et al. [41], who reported flower-like nanoparticle aggregates in algal-mediated synthesis. The presence of such high-surface-area structures enhances their potential for plant growth promotion, as suggested by Zaman et al. [42], who demonstrated improved nutrient uptake and root-shoot development in seedlings treated with nano-fertilizers.

The biochemical profile of *Halamphora subturgida* exhibited significant temporal variations following exposure to INP, reflecting a dynamic metabolic response. The chlorophyll content initially increased at 2 h, likely due to enhanced photosynthetic activity, but exhibited a progressive decline beyond 24 h, indicating oxidative stress-induced pigment degradation. This suggests that diatoms initially attempt to mitigate stress but succumb to prolonged exposure. Carotenoid content followed a similar trajectory, remaining stable up to 2 h before declining significantly after 12 h. Given the role of carotenoids in photoprotection, this depletion suggests increased oxidative stress, as seen in *Scenedesmus obliquus* exposed to metal nanoparticles [43]. The delayed reduction compared to chlorophyll indicates that carotenoids provide transient protection before degradation sets in. Carbohydrate content exhibited a biphasic response, with an initial peak at 12 h, possibly as a stress adaptation mechanism, followed by a decline at later stages. This trend aligns with observations by Biswas [44], who noted increased carbohydrate accumulation in diatoms under mild stress but depletion under prolonged exposure. The late-stage depletion suggests metabolic exhaustion, consistent with reduced photosynthetic efficiency. Protein levels demonstrated an adaptive rebound at 12–24 h, indicative of stress-mitigating protein synthesis. However, prolonged exposure led to significant degradation, likely due to proteolytic activity or impaired synthesis. This trend parallels findings in *Nannochloropsis* spp., where protein degradation was observed under oxidative stress conditions [45]. Lipid content exhibited an early accumulation phase that peaked at 6 h, followed by a decline, suggesting potential membrane remodeling or energy mobilization under stress. This suggests that initial lipid accumulation serves as a protective mechanism before oxidative stress leads to breakdown [46]. Carbon content, in contrast to other biochemical parameters, exhibited a steady increase over time, indicating continuous carbon fixation or accumulation of organic carbon compounds. This aligns with previous reports on diatom responses to nanoparticle exposure [47], suggesting that despite metabolic stress, diatoms maintain carbon sequestration, potentially as a survival strategy. Iron content showed a continuous upward trajectory, reaching levels more than tenfold higher than those of control samples. This progressive accumulation suggests active uptake and intracellular sequestration of iron, as similarly noted in different algal species [48]. The lack of decline further reinforces the hypothesis that diatoms effectively incorporate INPs into their metabolic framework.

The oxidative stress induced during INP synthesis significantly activated antioxidant enzymes, which played crucial roles in mitigating cellular damage and stabilizing nanoparticle formation. GR activity exhibited a steady increase, peaking at 48 h, indicating a prolonged role in cellular redox balance maintenance. GR is essential for regenerating reduced glutathione (GSH), which neutralizes reactive oxygen species (ROS) and prevents oxidative damage. This extended activation suggests a key role in post-synthesis stress recovery, ensuring sustained metabolic function in algal cells [49–51]. SOD activity peaked at 6 h, marking the highest level of superoxide radical detoxification. Since SOD catalyzes the dismutation of superoxide radicals into hydrogen peroxide, its rapid increase aligns with the active phase of INP formation, where oxidative stress is at its highest. The subsequent decline suggests either an adaptation to stress or enzyme depletion due to excessive ROS production [52]. CAT activity followed a similar pattern, peaking at 6 h to counteract the accumulation of hydrogen peroxide. As CAT converts hydrogen peroxide into water and oxygen, its peak suggests a critical detoxification phase during nanoparticle formation. The gradual decline post-12 h may indicate reduced ROS generation or enzyme inhibition under prolonged stress conditions [53]. POD activity reached its highest level at 12 h, suggesting a prolonged need for hydrogen peroxide detoxification beyond the early oxidative burst. POD plays a complementary role to CAT by utilizing hydrogen peroxide to oxidize various organic substrates, making it essential for sustained ROS regulation during INP synthesis [45,49]. APX peaked at 24 h, highlighting its role as a secondary defense mechanism in the ascorbate-glutathione cycle. APX is crucial for reducing hydrogen peroxide through ascorbate oxidation, ensuring long-term redox balance even after the primary oxidative stress phase. This delayed activation suggests its involvement in restoring cellular homeostasis post-nanoparticle formation [54].

Based on the observed enhancement in seedling growth and increased iron and silica accumulation, it is hypothesized that the diatom frustules act as a natural carrier, facilitating the gradual availability of iron nanoparticles while simultaneously supplying bioavailable silica to the developing seedlings. The combined presence of these two components may have contributed to the improved physiological performance observed in the present study. However, as nutrient-release kinetics and uptake mechanisms were not directly investigated, this proposed iron–silica synergistic effect should be regarded as a working hypothesis. Further studies involving nutrient-release analysis, transport pathways, and molecular investigations are required to validate the underlying mechanism. The observed morphological adaptations, spectral properties, and biochemical responses align well with existing literature, reinforcing the potential of diatoms in green nanotechnology.

5. Conclusions

This study demonstrates, for the first time, the potential of the marine diatom *Halamphora subturgida* as a biological platform for INP synthesis and its application as a NPF in rice. The diatom not only facilitated efficient intra- and extracellular nanoparticle formation but also exhibited distinct biochemical and antioxidant enzyme responses reflecting its metabolic adaptation during nanoparticle production. When applied to rice seedlings, INP-loaded diatoms consistently outperformed individual INP or diatom treatments, resulting in enhanced shoot and root growth, greater leaf development, higher biomass accumulation, increased chlorophyll content, and improved iron and silica uptake. These synergistic effects highlight the dual advantage of diatoms: providing biogenic silica and bioactive metabolites while stabilizing and delivering iron in a highly bioavailable form.

The findings underscore the promise of diatom-mediated nanofertilizers as sustainable alternatives to conventional chemical inputs. By combining micronutrient enrichment with natural structural support, INP-loaded diatoms offer a multifaceted strategy to improve crop vigor and resilience at early growth stages. Future studies should focus on field-scale validation, long-term soil interactions, and crop yield assessments to establish their broader applicability in sustainable agriculture.

Acknowledgements

The instrumental facilities have been supported by the Centre of Research for Nanoscience and Nanotechnology (CRNN), Bose Institute, and DST-FIST Level II, UGC-CAS programme, Department of Botany, University of Calcutta. The authors are thankful to Sweta Singh for her help during the experiment.

Author Contributions

Conceptualization, A.M.; Methodology, A.M. and R.B.; Software, A.M.; Validation, S.P. and R.P.; Formal Analysis, A.M. and R.B.; Investigation, A.M. and R.B.; Resources, A.M. and R.B.; Data Curation, A.M. and R.B.; Writing—Original Draft Preparation, A.M.; Writing—Review & Editing, A.M., R.B., S.P. and R.P.; Visualization, A.M. and R.P.; Supervision, R.P.; Funding Acquisition, A.M. and R.B.

Ethics Statement

Not applicable.

Informed Consent Statement

Not applicable.

Data Availability Statement

Data will be made available on request.

Funding

This work was supported by the University Grant Commission, Government of India, India by providing a fellowship to A.M. (fellow id—191520246470/CSIR-UGC NET DEC 2019). R.B. is indebted to the Swami Vivekananda Means cum merit Non-Net fellowship for providing financial assistance.

Declaration of Competing Interest

The authors declare that they have no known competing financial interests or personal relationships that could have appeared to influence the work reported in this paper.

Reference

1. Birla DS, Malik K, Sainger M, Chaudhary D, Jaiwal R, Jaiwal PK. Progress and challenges in improving the nutritional quality of rice (*Oryza sativa* L.). *Crit. Rev. Food Sci. Nutr.* **2017**, *57*, 2455–2481. DOI:10.1080/10408398.2015.1084992
2. Mondal A, Sabnam S, Paul S. *Sirocladium kumaoense* derived iron nanoparticles as a biopriming agent for enhanced early growth of rice seedlings. *J. Appl. Phycol.* **2025**, *37*, 4283–4297. DOI:10.1007/s10811-025-03680-0
3. Kılıç O, Boz İ, Eryılmaz GA. Comparison of conventional and good agricultural practices farms: A socio-economic and technical perspective. *J. Clean. Prod.* **2020**, *258*, 120666. DOI:10.1016/j.jclepro.2020.120666
4. Banerjee S, Lahiri R, Choudhury AK, Mondal A, Kim JW, MubarakAli D, et al. Unraveling the potential of cyanobacteria as food and investigating its production and nutritional properties. *Biocatal. Agric. Biotechnol.* **2024**, *62*, 103421. DOI:10.1016/j.bcab.2024.103421
5. Rout GR, Sahoo S. Role of iron in plant growth and metabolism. *Rev. Agric. Sci.* **2015**, *3*, 1–24. DOI:10.7831/ras.3.1
6. Mondal A, Paul S. Iron nanoparticles as efficient nano fertilizers for sustainable agriculture. *Discov. Plants* **2026**, *3*, 36. DOI:10.1007/s44372-026-00481-8
7. Saleem A, Zulfiqar A, Ali B, Naseeb MA, Almasaudi AS, Harakeh S. Iron Sulfate ($FeSO_4$) Improved Physiological Attributes and Antioxidant Capacity by Reducing Oxidative Stress of *Oryza sativa* L. Cultivars in Alkaline Soil. *Sustainability* **2022**, *14*, 16845. DOI:10.3390/su142416845
8. Mondal A, Mukherjee A, Pal R. Phycosynthesis of nanoiron particles and their applications—A review. *Biocatal. Agric. Biotechnol.* **2024**, *55*, 102986. DOI:10.1016/j.bcab.2023.102986

9. Rui M, Ma C, Hao Y, Guo J, Rui Y, Tang X, et al. Iron Oxide Nanoparticles as a Potential Iron Fertilizer for Peanut (*Arachis hypogaea*). *Front. Plant Sci.* **2016**, *7*, 815. DOI:10.3389/fpls.2016.00815
10. Dey I, Mondal A, Pal R. Sustainable waste valorization: Cyanobacteria-driven chromium nanoparticles for safe and contactless tomato preservation. *Proc. Indian Natl. Sci. Acad.* **2026**, *12*, 1–13. DOI:10.1007/s43538-026-00840-9
11. Chatterjee S, Mondal A, Saha S, Karmakar S, Chatterjee A, Paul S. Green-synthesized silver nanoparticles from *Leptolyngbya valderiana* selectively induce apoptotic death in lung adenocarcinoma. *Part. Sci. Technol.* **2026**, 1–14. DOI:10.1080/02726351.2026.2689639
12. Mondal A, Dey I, Mukherjee A, Ismail A, Satpati GG, Banerjee S, et al. *Spirulina* biomass loaded with iron nanoparticles: A novel biofertilizer for the growth and enrichment of iron content in rice plants. *Biocatal. Agric. Biotechnol.* **2024**, *61*, 103387. DOI:10.1016/j.bcab.2024.103387
13. Mondal A, Paul S, Pal R, Paul S. Nano iron loaded algal biomass: For better yield, amino acid and iron content in rice—A 'nano-phycofertilizer'. *Algal Res.* **2024**, *81*, 103573. DOI:10.1016/j.algal.2024.103
14. Rabiee N, Khatami M, Jamalipour Soufi G, Fatahi Y, Iravani S, Varma RS. Diatoms with Invaluable Applications in Nanotechnology, Biotechnology, and Biomedicine: Recent Advances. *ACS Biomater. Sci. Eng.* **2021**, *7*, 3053–3068. DOI:10.1021/acsbiomaterials.1c00475
15. Taiye MA, Hafida W, Kong F, Zhou C. A review of the use of rice husk silica as a sustainable alternative to traditional silica sources in various applications. *Environ. Prog. Sustain. Energy* **2024**, *43*, e14451. DOI:10.1002/ep.14451
16. Sabnam S, Mondal A, Paul S. Advancing seed priming with algal extracts: A review of mechanistic roles in seed germination and plant growth. *Explora Environ. Resour.* **2025**, *2*, 025120025. DOI:10.36922/EER025120025.
17. Bose R, Saha R, Chattopadhyay S, Pal R. Utilization of nanoporous biosilica of diatoms as a potential source material for fabrication of nanoelectronic device and their characterization. *J. Appl. Phycol.* **2020**, *32*, 3041–3049. DOI:10.1007/s10811-020-02134-z
18. Arnon DI. Copper enzymes in isolated chloroplasts. Polyphenoloxidase in *Beta vulgaris*. *Plant Physiol.* **1949**, *24*, 1–15. DOI:10.1104/pp.24.1.1
19. Rao AR, Dayananda C, Sarada R, Shamala TR, Ravishankar GA. Effect of salinity on growth of green alga *Botryococcus braunii* and its constituents. *Bioresour. Technol.* **2007**, *98*, 560–564. DOI:10.1016/j.biortech.2006.02.007
20. Parrish CC. Determination of Total Lipid, Lipid Classes, and Fatty Acids in Aquatic Samples. In *Lipids in Freshwater Ecosystems*; Arts MT, Wainman BC, Eds.; Springer: New York, NY, USA, 1999; pp. 4–20. DOI:10.1007/978-1-4612-0547-0_2
21. Walkley A, Black IA. An examination of the Degtjareff method for determining soil organic matter, and a proposed modification of the chromic acid titration method. *Soil Sci.* **1934**, *37*, 29–38. DOI:10.1097/00010694-193401000-00003.
22. Mohassab Y, Elzohiery M, Chen F, Sohn HY. Determination of Total Iron Content in Iron Ore and DRI: Titrimetric Method Versus ICP-OES Analysis. In *2016 EPD Congress*; Allanore A, Bartlett L, Wang C, Zhang L, Lee J, Eds.; John Wiley & Sons, Inc.: Hoboken, NJ, USA, 2016; pp. 125–133. DOI:10.1002/9781119274742.ch15
23. Owens C, Belcher R. A Colorimetric Micro-Method for the Determination of Glutathione. *Biochem. J.* **1965**, *94*, 705–711. DOI:10.1042/bj0940705
24. Schmedes A, Hølmer G. A new thiobarbituric acid (TBA) method for determining free malondialdehyde (MDA) and hydroperoxides selectively as a measure of lipid peroxidation. *J. Am. Oil Chem. Soc.* **1989**, *66*, 813–817. DOI:10.1007/BF02653674
25. Pérez F. Ascorbic acid and flavonoid-peroxidase reaction as a detoxifying system of H_2O_2 in grapevine leaves. *Phytochemistry* **2002**, *60*, 573–580. DOI:10.1016/S0031-9422(02)00146-2
26. Beauchamp C, Fridovich I. Superoxide dismutase: Improved assays and an assay applicable to acrylamide gels. *Anal. Biochem.* **1971**, *44*, 276–287. DOI:10.1016/0003-2697(71)90370-8
27. Sadasivam S. *Biochemical Method*; New Age International: New Delhi, India, 1996.
28. Mondal A, Paul S. Mitigating drought stress in Catharanthus roseus along with nano-iron enriched algal fertilizer application: A sustainable approach for enhanced growth and secondary metabolite production. *Comun. Sci.* **2025**, *16*, e4358. DOI:10.14295/cs.v16.4358
29. Dey S, Mondal A, Bhattacharya I, Pyne N, Paul S. Green synthesis of iron nanoparticles via *Rhizoclonum riparium* (Roth) Harvey: A promising nanotherapy against the promastigote forms of *Leishmania donovani* parasites. *Trends Phytochem. Res.* **2025**, *9*. DOI:10.57647/tpr.2025.0902.08
30. Banerjee S, Bhattacharya A, Roychoudhury P, Dasgupta AK, Dutta M, Pal R. *Arthrospira platensis* (Cyanobacteria)—A potential biofactory for fluoromagnetic nanoiron production. *Phycologia* **2021**, *60*, 62–72. DOI:10.1080/00318884.2020.1851010

31. Bensy ADV, Christobel GJ, Muthusamy K, Alfarhan A, Anantharaman P. Green synthesis of iron nanoparticles from *Ulva lactuca* and bactericidal activity against enteropathogens. *J. King Saud Univ. Sci.* **2022**, *34*, 101888. DOI:10.1016/j.jksus.2022.101888
32. Kiew PL, Fauzi NAM, Firdiani SA, Lam MK, Tan LS, Yeoh WM. Iron oxide nanoparticles derived from Chlorella vulgaris extract: Characterization and crystal violet photodegradation studies. *Prog. Energy Environ.* **2023**, *24*, 1–10. DOI:10.37934/progee.24.1.110
33. Chandran M, Yuvaraj D, Christudhas L, Ramesh KV. Bio synthesis of iron nanoparticles using the brown seaweed, *Dictyota dicotoma*. *Biotechnol. Indian J.* **2016**, *12*, 112. Available online: https://www.academia.edu/download/63429980/biosynthesis-of-iron-nanoparticles-using-the-brown-seaweed-dictyota-dicotoma20200526-31936-jpmzao.pdf (accessed on 10 August 2026).
34. Yew YP, Shameli K, Miyake M, Kuwano N, Bt Ahmad Khairudin NB, Bt Mohamad SE, et al. Green synthesis of magnetite (Fe_3O_4) nanoparticles using seaweed (*Kappaphycus alvarezii*) extract. *Nanoscale Res. Lett.* **2016**, *11*, 276. DOI:10.1186/s11671-016-1498-2
35. Khan Z, Ahmed AL-Thabaiti S, Hussain S. Nanoscale water soluble self-assembled zero-valent iron: Role of stabilizers in their morphology. *RSC Adv.* **2016**, *6*, 7267–7278. DOI:10.1039/C5RA17061C
36. Banerjee S, Banerjee I, Dutta M, Pal R. Fabrication of iron nanoparticles using *Leptolyngbya valderiana* and investigation of its Cr (VI) removal potential in the free and biomass associated forms. *Algal Res.* **2021**, *58*, 102373. DOI:10.1016/j.algal.2021.102373
37. Tungadi R. The effect of ultrasonication time on particle size, polydispersity index and stability evaluation of anthocyanin liposomes. *Univ. J. Pharm. Res.* **2024**, *9*, 8–13. DOI:10.22270/ujpr.v9i1.1056
38. Singh KM, Jha AB, Dubey RS, Sharma P. Nanoparticle-mediated mitigation of salt stress-induced oxidative damage in plants: insights into signaling, gene expression, and antioxidant mechanisms. *Environ. Sci. Nano* **2025**, *12*, 2983–3017. DOI:10.1039/D5EN00174A
39. Pestovsky YS, Martínez-Antonio A. The Use of Nanoparticles and Nanoformulations in Agriculture. *J. Nanosci. Nanotechnol.* **2017**, *17*, 8699–8730. DOI:10.1166/jnn.2017.15041
40. Kumar V, Singh R, Thakur S, Joshi KB, Vinayak V. Doping of magnetite nanoparticles facilitates clean harvesting of diatom oil as biofuel for sustainable energy. *Mater. Res. Express* **2018**, *5*, 045503. DOI:10.1088/2053-1591/aab86a
41. Patel AS, Juneja S, Kanaujia PK, Maurya V, Prakash GV, Chakraborti A, et al. Gold nanoflowers as efficient hosts for SERS based sensing and bio-imaging. *Nano-Struct. Nano-Objects* **2018**, *16*, 329–336. DOI:10.1016/j.nanoso.2018.09.001
42. Zaman W, Khalil AAK, Amin A, Ali S. Nanofabrication Techniques for Enhancing Plant–Microbe Interactions in Sustainable Agriculture. *Nanomaterials* **2025**, *15*, 1086. DOI:10.3390/nano15141086
43. Aizpuru A, González-Sánchez A. Traditional and new trend strategies to enhance pigment contents in microalgae. *World J. Microbiol. Biotechnol.* **2024**, *40*, 272. DOI:10.1007/S11274-024-04070-3
44. Biswas H. A story of resilience: Arctic diatom *Chaetoceros gelidus* exhibited high physiological plasticity to changing CO_2 and light levels. *Front. Plant Sci.* **2022**, *13*, 1028544. DOI:10.3389/fpls.2022.1028544
45. Yatipanthalawa B, Mienis E, Halim R, Foubert I, Ashokkumar M, Scales PJ, et al. Metabolic changes and biochemical degradation during dark anoxic incubation of *Nannochloropsis*: Implications for low-energy microalgal cell rupture. *Bioprocess Biosyst. Eng.* **2025**, *48*, 1399–1420. DOI:10.1007/s00449-025-03185-7
46. El-Beltagi HS, Mohamed HI. Reactive Oxygen Species, Lipid Peroxidation and Antioxidative Defense Mechanism. *Not. Bot. Hort Agrobot. Cluj-Napoca* **2013**, *41*, 44–57. DOI:10.15835/nbha4118929
47. Jia K, Sun C, Wang Y, Li X, Mu W, Fan Y. Effect of TiO_2 nanoparticles and multiwall carbon nanotubes on the freshwater diatom *Nitzschia frustulum*: Evaluation of growth, cellular components and morphology. *Chem. Ecol.* **2019**, *35*, 69–85. DOI:10.1080/02757540.2018.1528240
48. Liu F, Gledhill M, Tan QG, Zhu K, Zhang Q, Salaün P, et al. Phycosphere pH of unicellular nano- and micro-phytoplankton cells and consequences for iron speciation. *ISME J.* **2022**, *16*, 2329–2336. DOI:10.1038/s41396-022-01280-1
49. von Moos N, Slaveykova VI. Oxidative stress induced by inorganic nanoparticles in bacteria and aquatic microalgae—State of the art and knowledge gaps. *Nanotoxicology* **2014**, *8*, 605–630. DOI:10.3109/17435390.2013.809810
50. Dey I, Mondal A, Satpati GG, Pal R. Tannery wastewater remediation potential of cyanobacteria and algae with nutrient recovery, ecological monitoring and biomass valorization: A circular economy. *Next Chem. Eng.* **2025**, *1*, 100009. DOI:10.1016/j.nxcen.2025.100009
51. Dey I, Mondal A, Pal R. Algae-based systems for removal of emerging pollutant from sewage sludge. In *Biotechnological Removal of Emerging Pollutants from Wastewater Systems*; Springer Nature Singapore: Singapore, 2025; pp. 109–133. DOI:10.1007/978-981-96-3945-8_5

52. Ugya AY, Imam TS, Li A, Ma J, Hua X. Antioxidant response mechanism of freshwater microalgae species to reactive oxygen species production: A mini review. *Chem. Ecol.* **2020**, *36*, 174–193. DOI:10.1080/02757540.2019.1688308
53. Li J, Shi C, Wang X, Liu C, Ding X, Ma P, et al. Hydrogen sulfide regulates the activity of antioxidant enzymes through persulfidation and improves the resistance of tomato seedling to Copper Oxide nanoparticles (CuO NPs)-induced oxidative stress. *Plant Physiol. Biochem.* **2020**, *156*, 257–266. DOI:10.1016/j.plaphy.2020.09.020
54. Rao MJ, Duan M, Zhou C, Jiao J, Cheng P, Yang L, et al. Antioxidant Defense System in Plants: Reactive Oxygen Species Production, Signaling, and Scavenging During Abiotic Stress-Induced Oxidative Damage. *Horticulturae* **2025**, *11*, 477. DOI:10.3390/horticulturae11050477